Materials Chemistry and Physics 225 (2019) 159–168

Contents lists available at ScienceDirect

Materials Chemistry and Physics

journal homepage: www.elsevier.com/locate/matchemphys

Enhancement of mechanical properties of metallic glass nanolaminates via martensitic transformation: Atomistic deformation mechanism

Nicolas Amigo[a,*], Matias Sepulveda-Macias[b], Gonzalo Gutierrez[b]

[a] Núcleo de Matemáticas, Física y Estadística, Facultad de Estudios Interdisciplinarios, Universidad Mayor, Chile
[b] Grupo de NanoMateriales, Departamento de Física, Facultad de Ciencias, Universidad de Chile, Casilla 653, Santiago, Chile

HIGHLIGHTS

- Plasticity of Cu50Zr50/B2−CuZr nanolaminates under iso-stress and iso-strain are investigated.
- Martensitic transformation of the B2 phase enhances the strength of the nanolaminates.
- Iso-stress leads to void formation at the amorphous/crystalline interface.
- Iso-strain triggers B2 bands amorphization.

GRAPHICAL ABSTRACT

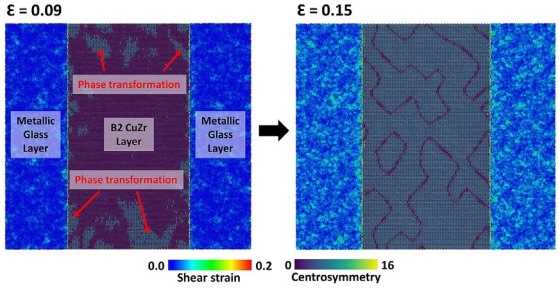

ARTICLE INFO

Keywords:
Metallic glasses
Martensitic transformation
Tensile test
Molecular dynamics simulation

ABSTRACT

Metallic glasses with embedded crystalline phases have been experimentally reported to exhibit enhanced mechanical properties. To further explore this observation, we employed molecular dynamics simulations to study $Cu_{50}Zr_{50}$/B2−CuZr nanolaminates subjected to tensile tests under iso–stress and iso–strain conditions. The onset of plasticity, martensitic transformation, and failure mechanisms were inspected at atomic level. It was found that most of the B2−CuZr phase undergoes martensitic transformation, enhancing the strength of the nanolaminate thanks to the second elastic regime developed in the crystalline layer. Interestingly, this transformation is promoted due to the rearrangement of Cu atoms at the amorphous/crystalline interface, without the direct influence of shear transformation zones. Regarding the failure mechanism, it was observed that it depends on the deformation condition: the iso–stress condition leads to void formation at the interface, whereas the iso–strain condition triggers B2 phase bands amorphization. Finally, tension–compression tests on $Cu_{50}Zr_{50}$/B2−CuZr nanolaminates under iso–strain revealed that the crystalline layer undergoes reversible B2–monoclinic transformation, decreasing the dissipated energy during mechanical loading when compared to the pure metallic glass sample.

1. Introduction

There has been an increasing interest to study bulk metallic glasses (MGs) in the last decade, due to their unique properties, such as high strength, hardness and corrosion resistance [1–3]. Recently, thin film metallic glasses with secondary crystalline phases have been proposed as candidates for enhancing the plasticity and ductility of micro–electromechanical systems [4]. In the case of $Cu_{1-x}Zr_x$ MGs, a promising procedure is to enhance ductility by preparing amorphous samples with a secondary Cu–crystalline phase or the binary B2−CuZr phase [5–7].

* Corresponding author. Núcleo de Matemáticas, Física y Estadística, Facultad de Estudios Interdisciplinarios, Universidad Mayor, Manuel Montt 318, Providencia, Santiago, Chile.
E-mail addresses: nico.amigo.a@gmail.com (N. Amigo), matsepmac@ug.uchile.cl (M. Sepulveda-Macias), gonzalogutierrez@uchile.cl (G. Gutierrez).

https://doi.org/10.1016/j.matchemphys.2018.12.050
Received 24 August 2018; Received in revised form 14 November 2018; Accepted 19 December 2018
Available online 24 December 2018
0254-0584/

These composites have proved to exhibit a combination of high yield strength and ductility, which is generally attributed to the interaction of plasticity between the amorphous and crystalline phases. Nevertheless, the exact mechanism is still not well understood.

Current experimental methods have allowed researchers to inspect shear bands propagation and crystal defects in MGs with secondary crystalline phases [8–10]. Unfortunately, these methods are limited in this regard to direct observations, being incapable to give more detailed information of the deformation process. Molecular dynamics (MD) simulations have demonstrated to be a suitable tool to explore the onset of dislocations, martensitic transformation (MT) and shear band nucleation at the atomic scale in amorphous–crystalline composites.

Previous studies have described the nucleation of shear transformation zones (STZs) and their interaction with partial dislocations in $Cu_{50}Zr_{50}$/Cu nanolaminates. Cui et al. [11] investigated the mechanical response of these nanolaminates under shear tests, finding that the interaction between dislocations and STZs prevents shear localization at the interface and promotes plastic deformation. Alishahi and Deng [12] studied the effect of the crystalline orientation in the plasticity of $Cu_{63}Zr_{37}$/Cu composites under tensile loading. The authors indicated that no significant differences were observed in the amorphous–crystalline interface energy for the different orientations. Interestingly, they reported that yielding may be initiated either by shear band or dislocation nucleation, depending on the crystalline orientation at the interface. In another work, Jian et al. [13] analyzed the plastic deformation of $Cu_{64}Zr_{36}$ nanoglasses with nanocrystalline Cu. The authors observed that an increasing fraction of the crystalline phase enhanced the tensile strength and reduced the ductility of the composite. Whereas there are more studies available in the literature about $Cu_{50}Zr_{50}$/Cu composites [14–19], only a few works can be found regarding the plastic deformation of $Cu_{50}Zr_{50}$/B2−CuZr nanolaminates at the atomic level.

It has been previously found that MT of B2−CuZr precipitates enhances the yield strength and ductility of $Cu_{1-x}Zr_x$ MGs [6,20,21]. Hence, there has been a wide interest to explore the interaction of both phases at the atomic level to understand its effect on the mechanical properties. Şopu et al. [22] carried out MD simulations of $Cu_{64}Zr_{36}$/B2−CuZr composite structures under uniaxial tensile tests. The B2 precipitates were inserted into the MG as [001] nanowires. The authors indicated that the MT drastically affected the strain localization, retarding the formation of a critical shear band (SB). Another work that has reported MT of the B2 phase is the one of Luan et al. [23], which studied plastic deformation of $Cu_{50}Zr_{50}$/B2−CuZr nanolaminates with different thicknesses. The authors found that the amorphous/crystalline interface blocked the propagation of the SB and MT provided homogeneous plastic deformation. Other authors have also investigated the effect of B2−CuZr precipitates without observing MT. The work of Brink et al. [24] described the interaction of a single SB with a spherical B2 precipitate, whereas Kalcher et al. [25] studied the creep behavior of $Cu_{64}Zr_{36}$ composites and Sepúlveda–Macías et al. [26] analyzed the size effect of spherical B2 precipitates on the yield strength of a $Cu_{50}Zr_{50}$ nanowire.

In this work, our aim was to further inspect the effect of MT on the onset of plasticity of $Cu_{50}Zr_{50}$/B2−CuZr composites. For this purpose, we carried out tensile tests on nanolaminates under iso–stress and iso–strain conditions considering different fractions of crystalline phase. These two conditions were employed as limiting cases to the different arrangement options of the crystalline phase. In the first part of this work, tensile tests on the $Cu_{50}Zr_{50}$/50%B2−CuZr composite under iso–stress and iso–strain were performed. An atomic level description of the plastic deformation and onset of failure was given in detail. Then, the deformation mechanisms were quantified by means of the atomic shear strain and centrosymmetry parameter, among other descriptors. In the final part, the reversibility of the martensitic transformation in the crystalline layer was analyzed. This paper was organized as follows: Section 2 explains the simulation procedure and the tools used for analysis, Section 3 presents and discusses the results, and Section 4 draws the conclusions.

2. Simulation details

Classical MD simulations must be carried out using an interatomic potential that accurately describes the interaction among atoms. Here, it was adopted the interatomic potential developed by Cheng et al. [27] for the CuZr system, which is based on the embedded atom method (EAM). In the EAM formalism, the potential energy of an embedded atom i is expressed as [28]

$$E_i = F_\alpha\left(\sum_{j\neq i}\rho_\beta(r_{ij})\right) + \frac{1}{2}\sum_{j\neq i}\phi_{\alpha\beta}(r_{ij}), \tag{1}$$

where α and β are the element types of atom i and a neighbor atom j, respectively. The charge density is represented by ρ_{ij} as a function of β and the embedding function is denoted as F_α. The term $\phi_{\alpha\beta}$ is the pair potential function between α and β.

The interatomic potential developed by Cheng et al. was fitted following different crystal structures obtained via ab initio MD. In addition, experimental elastic constants and phonon frequencies were also included. The fitting was validated against experimental and ab initio data, such as lattice parameters, cohesive energies, enthalpies of mixing, bulk modulus, elastic constants, etc [27]. The resulting interatomic potential has proved to describe accurately the CuZr system and it has been employed in several works, such as the study of icosahedral order [29], the glass transition and structural evolution [30], prediction of the shear modulus [31], plastic deformation in $Cu_{50}Zr_{50}$/Cu nanolaminates [15], among many others. The MD simulations in the present work were performed using the code LAMMPS [32].

The computational procedure to prepare the nanolaminates consisted of three different steps. In the first step, a well equilibrated amorphous $Cu_{50}Zr_{50}$ structure was created. For this purpose, a crystalline B2−CuZr system with dimensions $9.0 \times 3.8 \times 3.8$ nm_3 and lattice 0.32 nm, with periodic boundary conditions (PBC), was created. The system was relaxed in the NPT ensemble for 2 ns keeping the temperature and pressure fixed at 2000 K and 0 GPa, respectively. The integration timestep was set at 1 fs. Then, the system was cooled down to 10 K as described in our previous work [33]. The calculated cooling rate was $5 \times 10_{10}$ K/s. With this procedure, the amorphous $Cu_{50}Zr_{50}$ was obtained.

The objective in the second step was to prepare the MG–B2 nanolaminates. The MG prepared in the previous step was replicated eight times in the x–direction and z–direction, obtaining a new system with dimensions $52.4 \times 1.6 \times 52.4$ nm_3, containing ~258000 atoms. Then, a region ranging from $13.2 - 39.3$ nm in the x–direction, $0.0 - 1.6$ nm in the y–direction, and $0.0 - 52.4$ nm in the z–direction was removed. The B2−CuZr phase was created in the removed region, with the (100) plane in contact with the MG, obtaining an amorphous–crystalline composite nanolaminate with a 50% volume fraction of B2 phase. This volume fraction is given in relation to the total system volume. We refer to this system as the $Cu_{50}Zr_{50}$/50%B2−CuZr nanolaminate hereafter. The B2 layer was created with Zr atoms on its surface.

In the third step, the aim was to relax the amorphous/crystalline interface. The temperature of the nanolaminate was increased from 10 K to 1000 K at 10_{12} K/s using the Langevin thermostat, while keeping the pressure at 0 Pa with the Berendsen barostat. The system was kept at 1000 K for 100 ps, and then was cooled down to 10 K at 10^{12} K/s. Finally, the composite was relaxed at 10 K for 100 ps. Fig. 1 shows a zoom of the amorphous/crystalline interface.

For comparison purposes, three other samples were prepared. The first one consisted in the same system previously described, with a 50% volume fraction of B2 phase, but with Cu atoms located on its surface. The second and third samples corresponded to two nanolaminates with volume fractions of B2 phase of 20% and 80% with a Zr atoms interface,

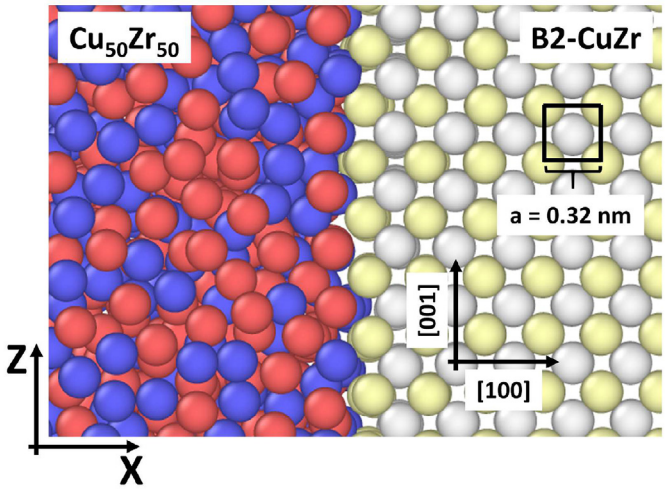

Fig. 1. $Cu_{50}Zr_{50}$ and B2−CuZr interface with Zr atoms at the interface. Zr atoms are represented by red and yellow, whereas Cu by blue and white. The lattice vectors of the crystalline phase are also presented. (For interpretation of the references to color in this figure legend, the reader is referred to the Web version of this article.)

which we call $Cu_{50}Zr_{50}$/20%B2−CuZr and $Cu_{50}Zr_{50}$/80%B2−CuZr respectively. The former has the B2 layer arranged from 21.0 to 31.4 nm in the *x*–direction, while the latter from 5.1 to 47.1 nm. In addition, two MG–$Cu_{50}Zr_{50}$ and B2−CuZr samples were prepared using the same dimensions and procedure. The B2−CuZr system was created with lattice vectors [100] along the x direction, [010] along the y direction, and [001] along the z direction.

All uniaxial tensile tests under iso–stress and iso–strain conditions were performed by loading the *x*–direction as shown in Fig. 2(a) and (b), respectively. The same procedure was repeated for the MG–$Cu_{50}Zr_{50}$ and B2−CuZr samples, where the latter was strained along the [100] direction. The strain was applied on the system by rescaling the position of all atoms each time step at 10_8 s_{-1} strain rate. This strain rate has been observed to produce similar results compared to other rates, without compromising severely the computational cost [34,35].

The temperature was kept constant at $T = 10$ K using the Langevin thermostat to ease analysis and inspection of the local atomic structure. PBC conditions were set in all directions. Several diagnostic tools were employed to analyze the simulations. In order to calculate the stress–-strain curve, the σ_{xx} component of the stress tensor was computed as [32]

$$\sigma_{ij} = -\frac{1}{V}\sum_{\alpha}\left(m^{\alpha}v_i^{\alpha}v_j^{\alpha} + \frac{1}{2}\sum_{\beta\neq\alpha} r_i^{\alpha\beta}F_j^{\alpha\beta}\right) \tag{2}$$

where V is the volume of the system, m^{α} is the mass of atom α, v_i^{α} and v_j^{α} are the i and j–component of velocity, respectively, $F_j^{\alpha\beta}$ is the i–component of the force between atoms α and β, and $r_i^{\alpha\beta}$ is the j–component of the distance between atoms α and β. In this equation, the first term is associated with the kinetic energy due to thermal vibration, while the second term with the potential energy due to the elastic deformation of the system.

The strain in the sample during a tensile test was calculated following the definition of the engineering strain

$$\varepsilon = \frac{L - L_0}{L_0}, \tag{3}$$

where L is the length of the system at any point during the test and L_0 is its original length.

The atomic structure of the MG layers was described by means of the local atomic shear strain given by Ref. [36],

$$\eta^{\text{Mises}} = \sqrt{\eta_{yz}^2 + \eta_{xz}^2 + \eta_{xy}^2 + \frac{(\eta_{yy} - \eta_{zz})^2 + (\eta_{xx} - \eta_{zz})^2 + (\eta_{xx} - \eta_{yy})^2}{6}}, \tag{4}$$

where $\eta_{\alpha\beta}$ are the components of the strain tensor of atom i. Once η^{Mises} was calculated, we were able to determine the shear strain distribution in all samples. This was quantified by means of the "degree of strain localization" parameter [37], defined as

$$\psi = \sqrt{\frac{1}{N}\sum_{i=1}^{N}(\eta_i^{\text{Mises}} - \eta_{\text{ave}}^{\text{Mises}})^2}, \tag{5}$$

where N is the total number of atoms, η_i^{Mises} is the von Mises strain of atom i, and $\eta_{\text{ave}}^{\text{Mises}}$ is the average von Mises strain of all atoms. The interpretation of this parameter is that a larger value of ψ implies a higher degree of strain localization.

The atomic structure of the B2 layers and its change of phase was described using the centrosymmetry parameter (CSP) [38], which is defined for atom i as

$$c_i = \sum_{j=1}^{N/2} |\vec{R}_j + \vec{R}_{j+N/2}|^2, \tag{6}$$

where N is the number of nearest neighbors of atom i, $\vec{R}_j$ and $\vec{R}_{j+N/2}$ are the vectors from atom i to a pair of opposite nearest neighbors. Note that since the B2–phase can be regarded as a BCC structure, the number of nearest neighbors is $N = 8$. In this study, $0.0 < c_i < 0.6$ represented the B2 structure, while $1.0 < c_i < 3.5$ and $6.5 < c_i < 8.5$ corresponded to

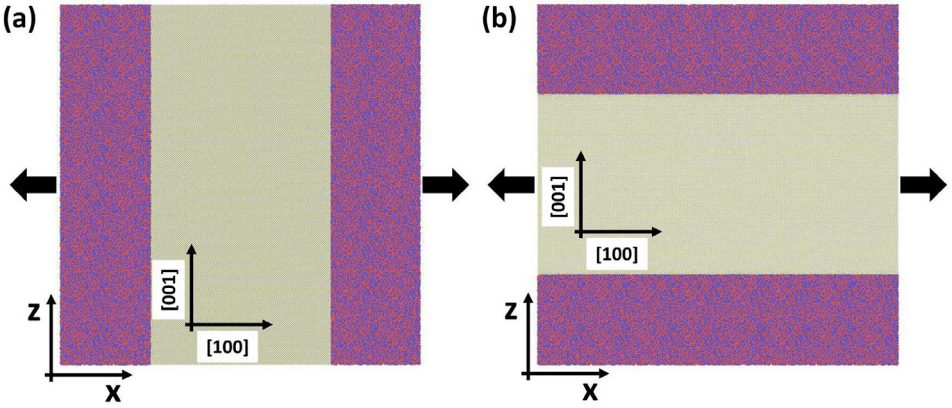

Fig. 2. $Cu_{50}Zr_{50}$/20%B2−CuZr composite. The tensile loading was applied along the *x* direction. (a) Composite under iso–stress and (b) iso–strain conditions. The lattice vectors of the crystalline phase are also presented.

Zr and Cu atoms in the monoclinic structure, respectively. This monoclinic structure was previously shown in our previous work [34]. The simulation results were visualized using the software OVITO [39].

3. Results

The $Cu_{50}Zr_{50}$/B2−CuZr nanolaminates were prepared in such a way that only Zr or Cu atoms of the crystalline phase were in contact with the amorphous phase. For instance, the case of Zr atoms on the contact surface is shown in Fig. 1. In order to explore the influence of a Zr or a Cu contact interface, the energy difference as well as the stress–strain curves of both cases were compared. The interface energy of the composites was calculated as

$$\gamma_{int} = (E_{A/C} - E_{amor} - E_{crys})/S_{int}, \quad (7)$$

where $E_{A/C}$ is the total energy of the amorphous/crystalline system, computed as the sum of the potential energy of all atoms after relaxation. Analogously, E_{amor} and E_{crys} correspond to the total energy of the amorphous and crystalline layers with PBC, respectively. S_{int} represents the total interface cross–sectional area. The obtained values for γ_{int} were $-0.88\ J/m_2$ and $-0.85\ J/m_2$, for the samples with Zr and Cu atoms on the contact surface, respectively. The difference between both quantities was 0.9%, indicating that the atom type at the surface does not affect significantly the energy landscape at the interface.

The two samples were also subjected to tensile tests under iso–stress condition to investigate the effect of the interface on the stress–strain curve. The results are shown in Fig. 3. Both curves have the same behavior during the elastic and plastic regime. Small differences appear during the onset of fracture ($\varepsilon = 0.19$), where the sample with Cu atoms at the amorphous/crystalline interface displays an ultimate tensile strength only 0.26% higher than the one of the other system. Overall, placing Zr or Cu atoms on the contact surface has no significant impact on the mechanical behavior of both samples. Therefore, in the rest of this work we only consider systems where Zr atoms are located on the contact surface.

3.1. Tensile tests under iso–stress and iso–strain conditions

Uniaxial tensile tests were carried out for the $Cu_{50}Zr_{50}$/50% B2−CuZr nanolaminate, under iso–stress and iso–strain conditions. The test was also performed for the MG–$Cu_{50}Zr_{50}$ and the crystalline B2−CuZr samples. The resulting stress–strain curves are shown in Fig. 4. Both nanolaminates exhibit elastic behavior up to $\varepsilon = 0.08$. A bump is observed at $\varepsilon = 0.09$ for the iso–stress condition, at $\varepsilon = 0.10$ for the iso–strain condition, and at $\varepsilon = 0.10$ for the B2−CuZr sample, as can be seen in the inset of Fig. 4. Then, the stress increases until a maximum value, where the failure begins. It is important to note that both composites present enhanced strength when compared to the pure MG system, which is in agreement with experimental results [6,7]. The Young's modulus E (estimated as the slope of the curve between $\varepsilon = 0.00$ and $\varepsilon = 0.01$), the yield stress (measured at $\varepsilon = 0.002$ offset), the bump stress σ_b (measured before the abrupt change of slope), and the ultimate tensile stress σ_u (computed as the maximum stress) of all cases are presented in Table 1. It is interesting to note that the yield stress of the B2−CuZr sample is much higher compared to the others, because this system exhibits a complete elastic behavior up to $\varepsilon = 0.09$. In addition, there is no σ_b calculated for the MG–$Cu_{50}Zr_{50}$ since its curve does not present any bump.

An atomic level picture for the nanocomposite under iso–stress is given in Fig. 5, where the MG and the crystalline phase are colored according to the atomic shear strain and the centrosymmetry parameter, respectively. Fig. 5(a) shows the nanolaminate at $\varepsilon = 0.09$, just when the bump in the stress–strain curve takes place. It is seen that STZs are nucleated homogeneously in the amorphous matrix, whereas {110} transformation planes from B2 to monoclinic phase are promoted at the interface (atoms in green and enclosed by red lines), which was previously reported in the literature but not described in detail [40]. As the strain increases, these transformation bands coalesce, and the crystalline layer is dominated by monoclinic structure, except for narrow bands of B2 phase, as shown in Fig. 5(b). At $\varepsilon = 0.19$, voids begin to nucleate at the amorphous/crystalline interface and the B2 bands of the crystalline structure undergo amorphization, as depicted in Fig. 5(c).

In the case of iso–strain condition, the formation and propagation of

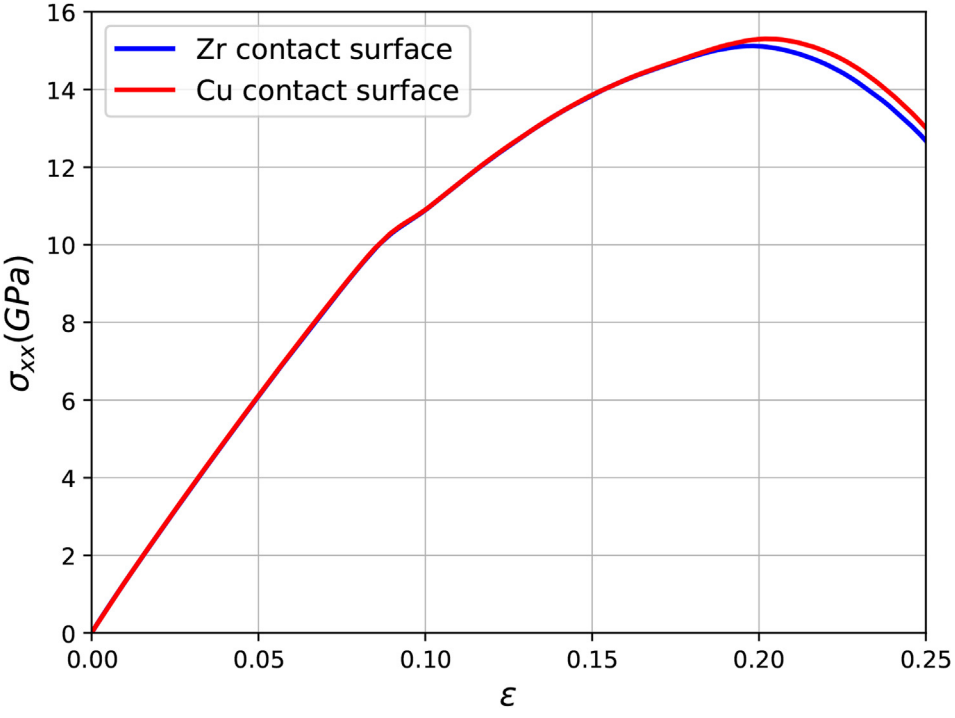

Fig. 3. Stress–strain curves for $Cu_{50}Zr_{50}$/50% B2−CuZr nanolaminates under iso–stress where the amorphous/crystalline contact surface is composed of Zr atoms (blue curve) and Cu atoms (red curve). (For interpretation of the references to color in this figure legend, the reader is referred to the Web version of this article.)

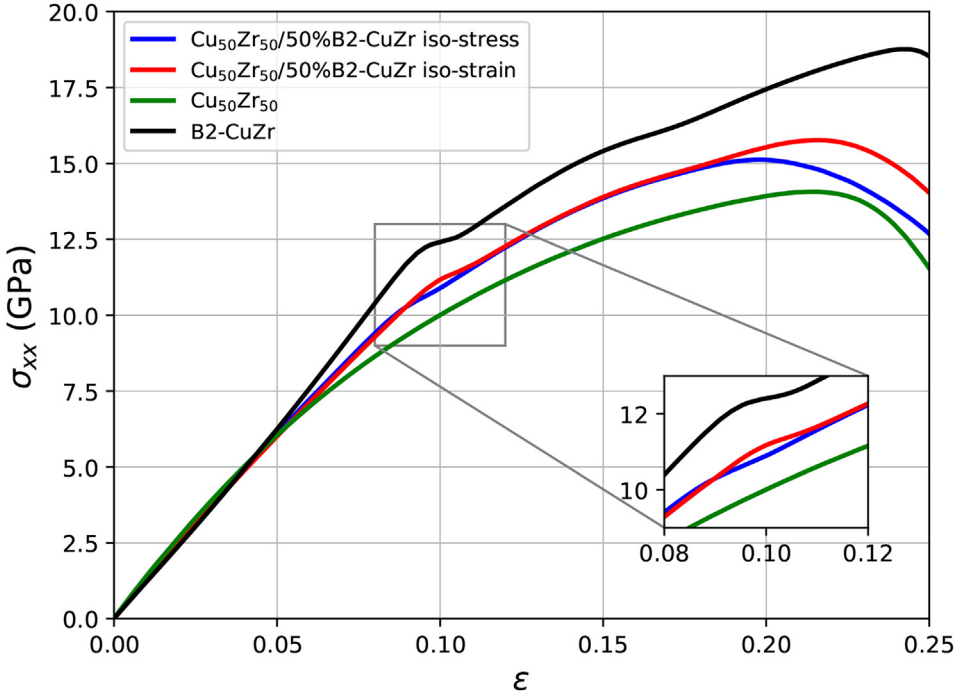

Fig. 4. Stress–strain curves for the $Cu_{50}Zr_{50}$/50%B2−CuZr nanolaminate under iso–stress and iso–strain, and for the pure MG–$Cu_{50}Zr_{50}$ and B2−CuZr samples.

Table 1
Young's modulus, E, yield stress, σ_y, and ultimate tensile stress, σ_u, of $Cu_{50}Zr_{50}$/50%B2−CuZr under iso–stress and iso–strain, as well as for MG–$Cu_{50}Zr_{50}$ and B2−CuZr.

Condition	E (GPa)	σ_y (GPa)	σ_b (GPa)	σ_u (GPa)
Iso–stress	133.84	3.80	10.31	15.01
Iso–strain	135.35	3.31	11.17	15.74
MG–$Cu_{50}Zr_{50}$	144.76	3.25	–	14.06
B2−CuZr	123.59	12.49	12.35	18.81

transformation bands is also observed, as well as STZs nucleation and narrow bands of B2 phase ((Fig. 6(a) and (b)). However, some differences can be distinguished. The bump in the stress–strain curve is exhibited close to $\varepsilon = 0.10$, the onset of failure is at a higher strain ($\varepsilon = 0.22$), the amorphization process is stronger, and the void formation at the interface is almost negligible (Fig. 6(c)).

3.2. Deformation mechanisms

The simulations allowed us to uncover how operate both iso–stress and iso–strain conditions at the atomic level. We will see that there are two different, unrelated deformation mechanisms during these tests, namely, martensitic transformation (MT) and shear transformation zones (STZs).

Regarding the MT in the nanolaminate under iso–stress, one can observe that some Cu atoms are closer to each other according to the progress of the deformation process, labeled as “d” in Fig. 7(a). This behavior constitutes the onset of the monoclinic bands, as shown in Fig. 7(b). Hence, the MT is promoted due to the rearrangement of Cu atoms close to the contact surface, without the influence of STZs. The transformations bands ultimately coalesce and dominate the crystalline phase, coexisting with thin, narrow B2 phase paths. The same phenomenon is found in the nanolaminate under iso–strain.

The distribution of STZs in the nanolaminate under both tensile tests was quantified by means of the ψ parameter. The results were compared with the case of pure MG, which are shown in Fig. 8. It is observed that

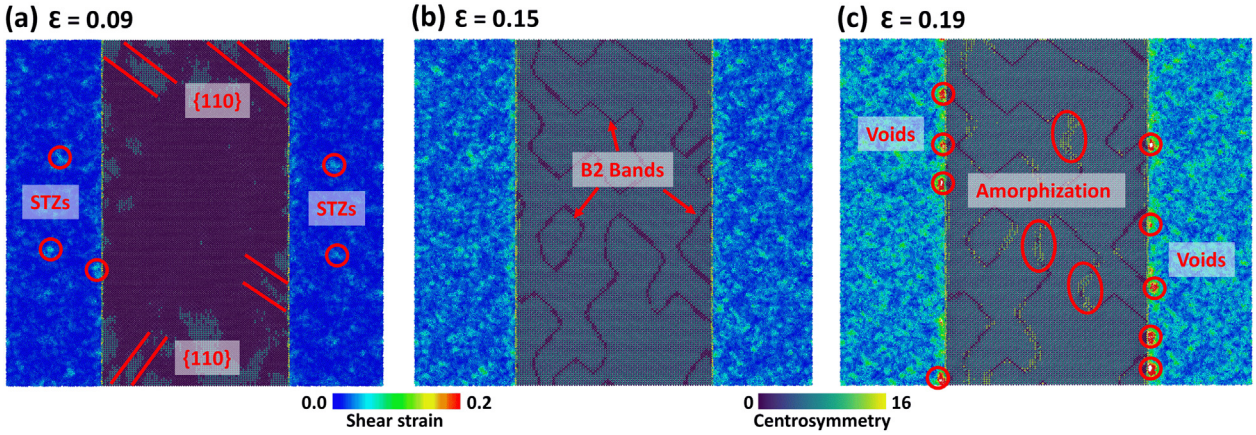

Fig. 5. $Cu_{50}Zr_{50}$/50%B2−CuZr nanolaminate under iso–stress at (a) $\varepsilon = 0.09$, (b) $\varepsilon = 0.15$ and (c) $\varepsilon = 0.19$. The amorphous and crystalline phase are colored according to the local atomic shear strain and centrosymmetry parameter, respectively.

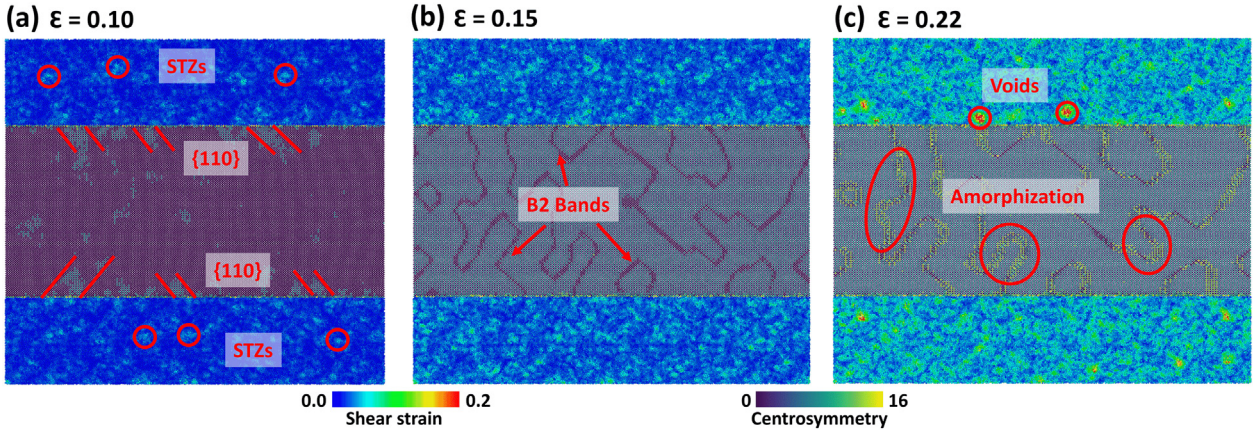

Fig. 6. $Cu_{50}Zr_{50}$/50%B2−CuZr nanolaminate under iso–strain at (a) $\varepsilon = 0.10$, (b) $\varepsilon = 0.15$ and (c) $\varepsilon = 0.22$. The amorphous and crystalline phase are colored according to the local atomic shear strain and centrosymmetry parameter, respectively.

all samples have almost the same ψ value until $\varepsilon = 0.06$, and then, ψ increases earlier in the composites compared to the pure MG sample, meaning that the crystalline phase localizes the strain field. Following the work of Sepúlveda–Macías et al. [26], this phenomenon should decrease the mechanical strength of the systems compared to the pure MG. However, the opposite behavior is observed from the stress–strain curves in Fig. 4, since the B2 phase undergoes MT, reaching its second elastic regime and thus, enhancing the strength of the nanolaminates. This transformation was not observed in the work of Sepúlveda–Macías et al., possibly due to the relaxation procedure when preparing the samples. The authors simply relaxed the systems at 300 K for 100 ps. In contrast, here the samples were annealed at 1000 K, and then they were quenched to 10 K, allowing the amorphous/crystalline interface to become more relaxed.

In Section 3.1 it was described that the failure of the nanolaminate varied, depending on whether the iso–stress or the iso–strain condition was applied. The former promotes failure by means of void formation at the amorphous/crystalline interface, while the latter by means of amorphization of the remaining B2 phase bands. In order to understand the differences in both cases, the degree of strain localization was compared. From Fig. 8, the iso–stress condition leads to more localized strain fields, which are concentrated at the interface (see Fig. 5(b)), leading to void nucleation (see Fig. 5(c)). To shed light to this point, the potential energy profile was calculated along the x direction (see Fig. 2(a)) in the composite under iso–stress and along the z direction (see Fig. 2(b)) in the composite under iso–strain. The results are shown in Fig. 9. It is observed that there are peaks in potential energy at $x \approx 0.20$ nm, $x \approx 0.80$ nm for the nanolaminate under iso–stress, and at $z \approx 0.25$ nm, $z \approx 0.75$ nm for the composite under iso–strain, corresponding to the amorphous/crystalline interfaces. For the sample under iso–stress, the interface energy is higher compared to the case under iso–strain, indicating that the atoms are more distant from each other, easing the void formation process. On the other hand, the sample under iso–strain fails due to B2 bands amorphization (Fig. 6(c)). This observation was quantified by calculating the fraction of atoms in the crystalline phase with centrosymmetry deviation above 12, resulting in the curves presented in Fig. 10. As expected, the sample under iso–strain has a higher fraction of atoms with $c_i > 12$ ($\varepsilon > 0.18$) than the iso–stress case, which represents a stronger amorphization of B2 bands.

3.3. Reversibility of $Cu_{50}Zr_{50}$/50%B2−CuZr nanolaminates

The crystalline phase of the composite exhibits MT from B2 phase to monoclinic structure. A natural question that raises from this observation is whether the transformation is reversible or not. In order to clarify this matter, three nanolaminates with three different B2 volume fractions, $Cu_{50}Zr_{50}$/20%B2−CuZr, $Cu_{50}Zr_{50}$/50%B2−CuZr and $Cu_{50}Zr_{50}$/80%B2−CuZr, were subjected to tension–compression tests under iso–strain condition. For comparison purposes, the test was also performed on the pure MG sample. Fig. 11 shows the stress–strain curves of the four cases. As expected, the pure MG sample presents the lowest yield strength, whereas the $Cu_{50}Zr_{50}$/80%B2−CuZr composite exhibits the highest. Moreover, this nanolaminate exhibits a noticeable bump at the onset of the MT ($\varepsilon = 0.10$). During the compression tests, all

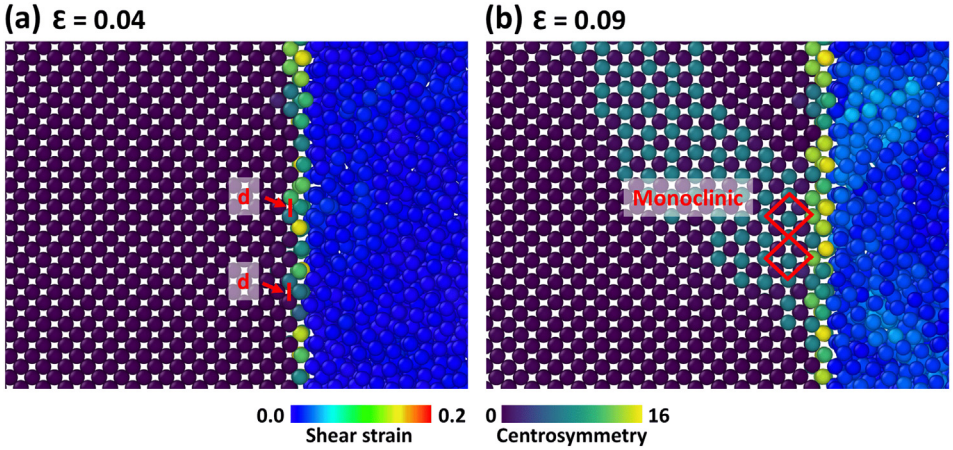

Fig. 7. Amorphous/crystalline interface and monoclinic structure transformation at (a) $\varepsilon = 0.04$ where some Cu atoms are closer to each other. In (b) nucleation of a transformation band at $\varepsilon = 0.09$.

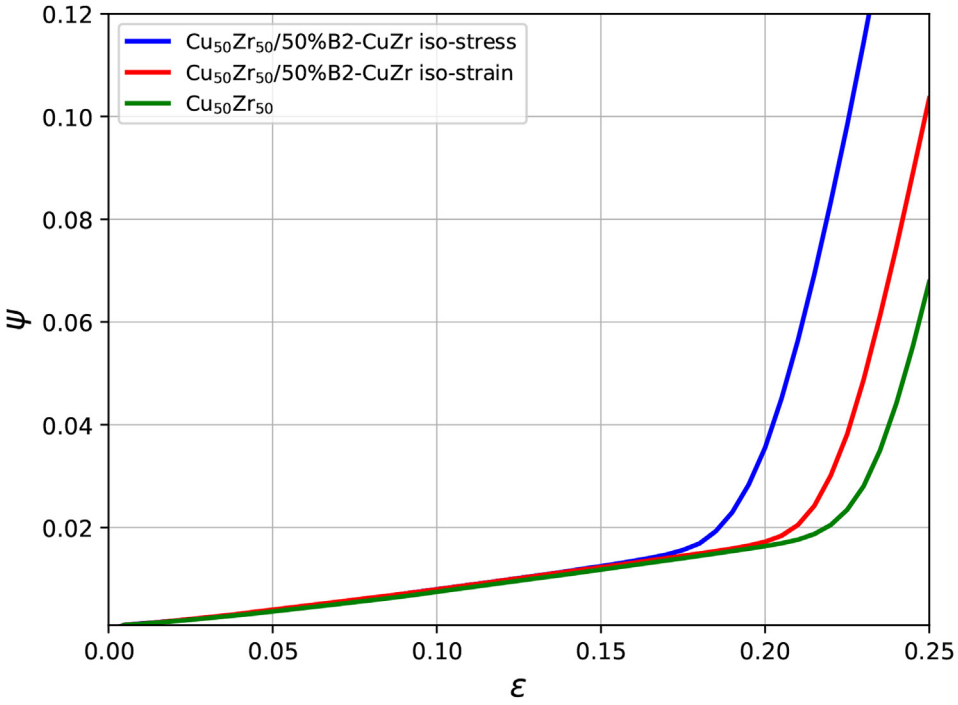

Fig. 8. Degree of strain localization for $Cu_{50}Zr_{50}$/50%B2−CuZr under iso–stress, iso–strain and pure MG.

crystalline phases underwent a reversible MT from monoclinic structure to B2 phase. Nevertheless, at the end of these tests, none of the samples achieved $\varepsilon = 0$ at $\sigma = 0$, since the transition from elastic to plastic regime of the MG layer is not a reversible process, as seen in Fig. 12 for the $Cu_{50}Zr_{50}$/50%B2−CuZr nanolaminate after unloading. Table 2 summarizes the remaining strains ε_r and the dissipated energies E_d for the four samples. It is observed that the lowest dissipated energy corresponds to the $Cu_{50}Zr_{50}$/80%B2−CuZr nanolaminate, whereas the highest to the pure MG sample. Hence, the higher the fraction of the B2 phase, the lower the dissipated energy in the system.

4. Conclusions

Uniaxial tensile tests have been carried out to study the plastic behavior of $Cu_{50}Zr_{50}$/B2−CuZr nanolaminates. The tests were performed under iso–stress and iso–strain conditions. Shear transformation zones and martensitic transformation were inspected and analyzed in detail. Three main features were observed in this work:

1. The $Cu_{50}Zr_{50}$/50%B2−CuZr nanolaminate under iso–stress and iso–strain exhibited higher degree of strain localization than the

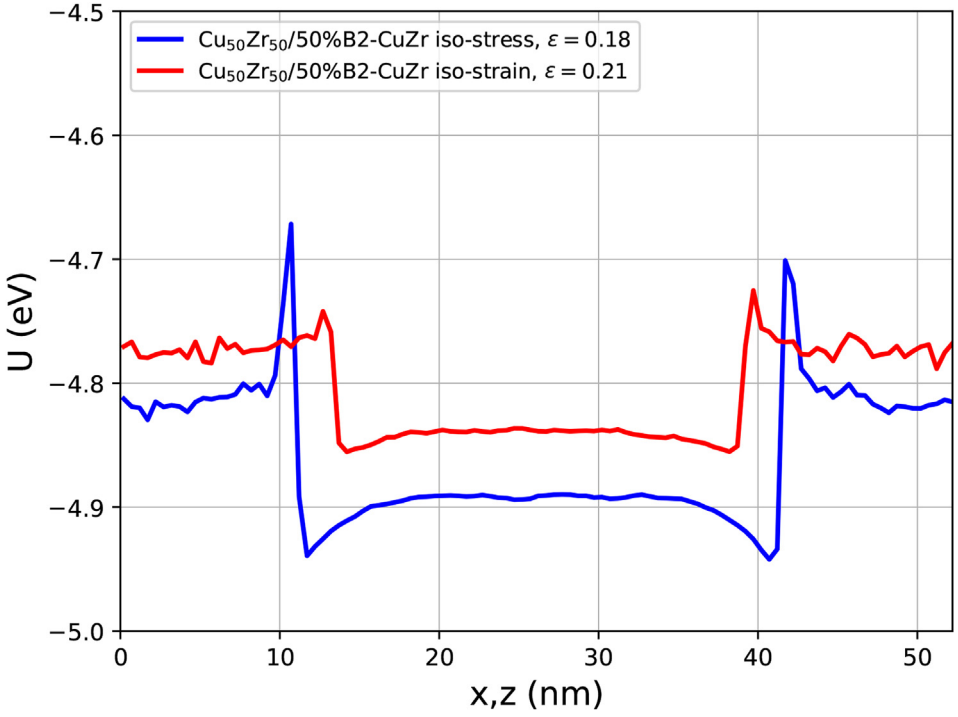

Fig. 9. Energy profiles across the amorphous/crystalline/amorphous layers prior to failure.

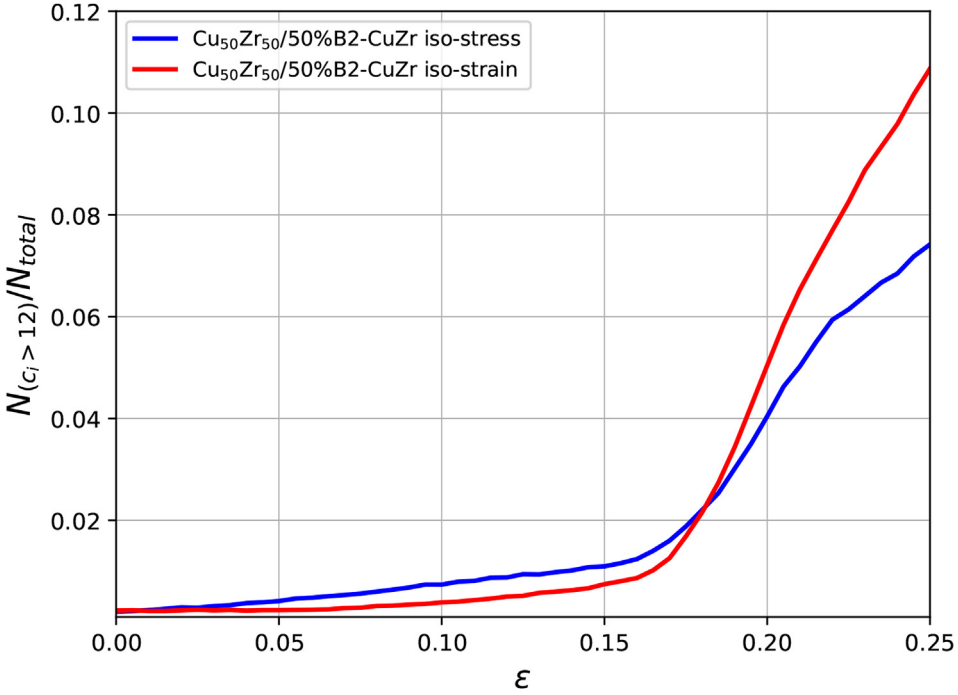

Fig. 10. Fraction of atoms of the crystalline phase with high centrosymmetry deviation ($c_i > 12$) for $Cu_{50}Zr_{50}$/50%B2−CuZr under iso–stress and iso–strain.

pure MG sample. However, thanks to the martensitic transformation, the crystalline layer reached a second elastic regime, enhancing the strength of the whole composite.

2. The onset of failure in the nanolaminate under iso–stress was triggered by void nucleation at the amorphous/crystalline interface. In contrast, the failure in the nanolaminate under iso–strain was initiated by amorphization of B2 phase bands in the crystalline matrix.
3. All of the composites, with different crystalline volume fractions, showed martensitic transformation from B2 to monoclinic structure during tension, and reversible transformation from monoclinic to B2 phase during compression. Furthermore, the composite with the highest crystalline fraction presented the lowest dissipated energy during the test.

Overall, it has been shown that the martensitic transformation of the B2−CuZr phase improved the strength of the MG–$Cu_{50}Zr_{50}$, and decreased the dissipated energy during mechanical loadings. Since these results are in agreement with experimental observations, molecular

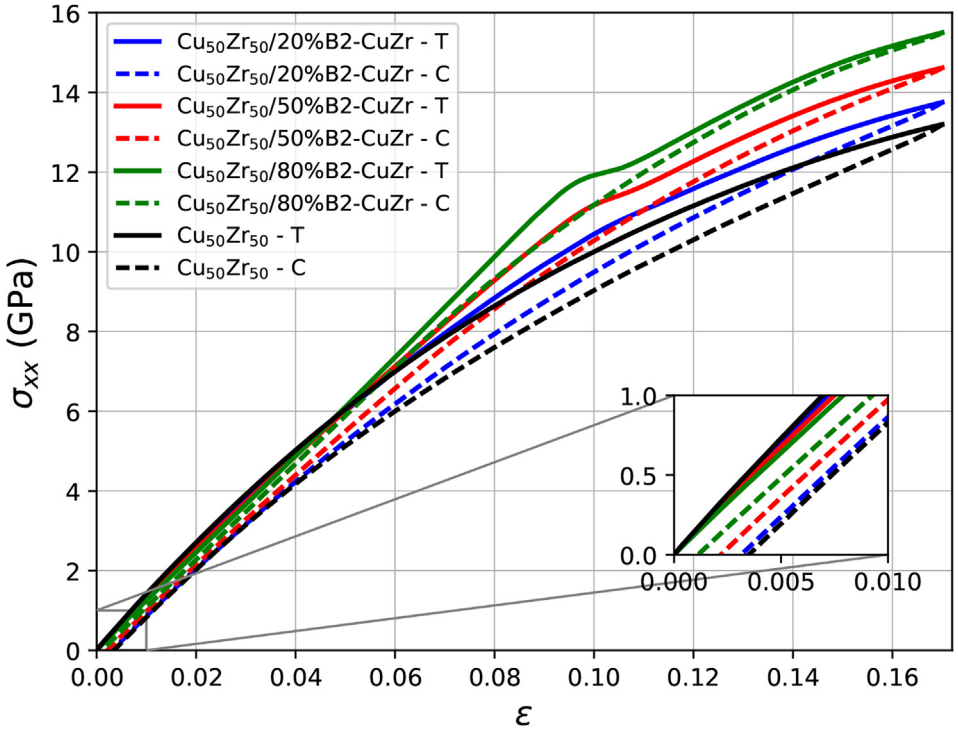

Fig. 11. Tension–compression tests under iso–strain for the $Cu_{50}Zr_{50}$/B2−CuZr nanolaminate with three different B2 volume fractions and pure MG sample.

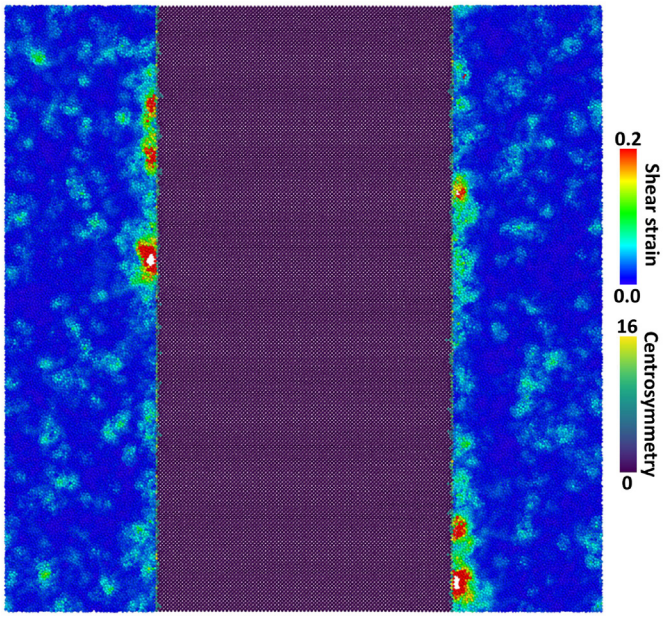

Fig. 12. $Cu_{50}Zr_{50}$/50%B2−CuZr nanolaminate after unloading, where the crystalline phase underwent a reversible martensitic transformation from monoclinic to B2 structure. The amorphous phase remains with residual strain.

Table 2
Remaining strains ε_r and dissipated energies E_d in all samples.

Nanolaminate	ε_r	E_d (MJ/m$_3$)
$Cu_{50}Zr_{50}$	0.0035	131.28
$Cu_{50}Zr_{50}$/20%B2−CuZr	0.0031	113.89
$Cu_{50}Zr_{50}$/50%B2−CuZr	0.0021	84.02
$Cu_{50}Zr_{50}$/80%B2−CuZr	0.0011	51.10

dynamics simulations can help to further understand the amorphous/crystalline interactions in complex composites.

Acknowledgements

NA thanks to CONICYT PhD fellowship No. 21151448. M.S-M. thanks to CONICYT Ph.D. fellowship No. 21140904. G.G. thanks the partial support to grant FONDECYT 1171127.

References

[1] W.L. Johnson, Bulk metallic glasses a new engineering material, Curr. Opin. Solid State Mater. Sci. 1 (3) (1996) 383–386 https://doi.org/10.1016/S1359-0286(96)80029-5 http://www.sciencedirect.com/science/article/pii/S1359028696800295.
[2] M. Telford, The case for bulk metallic glass, Mater. Today 7 (3) (2004) 36–43 https://doi.org/10.1016/S1369-7021(04)00124-5 http://www.sciencedirect.com/science/article/pii/S1369702104001245.
[3] A.L. Greer, Metallic glasseson the threshold, Mater. Today 12 (12) (2009) 14–22 https://doi.org/10.1016/S1369-7021(09)70037-9 http://www.sciencedirect.com/science/article/pii/S1369702109700379.
[4] J.L. Zhe Fan, Y. Yang, J. Wang, Q. Li, S. Xue, H. Wang, J. Lou, X. Zhang, Ductile fracture of metallic glass nanolaminates, Adv. Mater. Interface 4 (1700510) (2017) 1–9, https://doi.org/10.1002/admi.201700510.
[5] D.C. Hofmann, J.-Y. Suh, A. Wiest, G. Duan, M.-L. Lind, M.D. Demetriou, W.L. Johnson, Designing metallic glass matrix composites with high toughness and tensile ductility, Nature 451 (February) (2008) 1085–1089, https://doi.org/10.1038/nature06598.
[6] S. Pauly, S. Gorantla, G. Wang, U. Kühn, J. Eckert, Transformation-mediated ductility in cuzr-based bulk metallic glasses, Nat. Mater. 9 (6) (2010) 473–477, https://doi.org/10.1038/nmat2767 https://doi.org/10.1038/nmat2767.
[7] Y. Wu, H. Wang, H. Wu, Z. Zhang, X. Hui, G. Chen, D. Ma, X. Wang, Z. Lu, Formation of cuzral bulk metallic glass composites with improved tensile properties, Acta Mater. 59 (8) (2011) 2928–2936 https://doi.org/10.1016/j.actamat.2011.01.029 http://www.sciencedirect.com/science/article/pii/S1359645411000358.
[8] M. Liu, J. Huang, H. Chou, Y. Lai, C. Lee, T. Nieh, A nanoscaled underlayer confinement approach for achieving extraordinarily plastic amorphous thin film, Scripta Mater. 61 (8) (2009) 840–843 https://doi.org/10.1016/j.scriptamat.2009.07.010 http://www.sciencedirect.com/science/article/pii/S1359646209004606.
[9] W. Guo, E.A. Jägle, P.-P. Choi, J. Yao, A. Kostka, J.M. Schneider, D. Raabe, Shear-induced mixing governs codeformation of crystalline-amorphous nanolaminates, Phys. Rev. Lett. 113 (2014) 035501, , https://doi.org/10.1103/PhysRevLett.113.035501 https://link.aps.org/doi/10.1103/PhysRevLett.113.035501.
[10] Y. Cui, O.-T. Abad, F. Wang, P. Huang, T.-J. Lu, K.-W. Xu, J. Wang, Plastic deformation modes of cuzr/cu multilayers, Sci. Rep. 6 (2016) 23306, https://doi.org/10.1038/srep23306 https://www.nature.com/articles/srep23306.
[11] Y. Cui, Y. Shibutani, S. Li, P. Huang, F. Wang, Plastic deformation behaviors of amorphous-cu50zr50/crystalline-cu nanolaminated structures by molecular dynamics simulations, J. Alloy. Comp. 693 (2017) 285–290 https://doi.org/10.1016/j.jallcom.2016.09.184 http://www.sciencedirect.com/science/article/pii/S0925838816329383.
[12] E. Alishahi, C. Deng, Orientation dependent plasticity of metallic amorphous-crystalline interface, Comput. Mater. Sci. 141 (2018) 375–387 https://doi.org/10.1016/j.commatsci.2017.09.057 http://www.sciencedirect.com/science/article/pii/S0927025617305451.
[13] W.R. Jian, L. Wang, X.H. Yao, S.N. Luo, Balancing strength, hardness and ductility of cu 64 zr 36 nanoglasses via embedded nanocrystals, Nanotechnology 29 (2) (2018) 025701http://stacks.iop.org/0957-4484/29/i=2/a=025701.
[14] W.R. Jian, L. Wang, B. Li, X.H. Yao, S.N. Luo, Improved ductility of cu 64 zr 36 metallic glass/cu nanocomposites via phase and grain boundaries, Nanotechnology 27 (17) (2016) 175701 http://stacks.iop.org/0957-4484/27/i=17/a=175701.
[15] Y. Luan, C. Li, D. Zhang, J. Li, X. Han, J. Li, Plastic deformation mechanisms and size effect of cu50zr50/cu amorphous/crystalline nanolaminate: a molecular dynamics study, Comput. Mater. Sci. 129 (2017) 137–146 https://doi.org/10.1016/j.commatsci.2016.12.003 http://www.sciencedirect.com/science/article/pii/S0927025616306176.
[16] H. Song, J. Xu, Y. Zhang, S. Li, D. Wang, Y. Li, Molecular dynamics study of deformation behavior of crystalline cu/amorphous cu50zr50 nanolaminates, Mater. Des. 127 (2017) 173–182 https://doi.org/10.1016/j.matdes.2017.04.077 http://www.sciencedirect.com/science/article/pii/S0264127517304343.
[17] L. Zhao, K. Chan, S. Chen, Atomistic deformation mechanisms of amorphous/polycrystalline metallic nanolaminates, Intermetallics 95 (2018) 102–109 https://doi.org/10.1016/j.intermet.2018.01.023 http://www.sciencedirect.com/science/article/pii/S0966979517309718.
[18] H. Song, S. Li, M. An, Q. Deng, Y. Li, Effect of crystal phase on shear bands initiation and propagation behavior in metallic glass matrix composites, Comput. Mater. Sci. 150 (2018) 42–46 https://doi.org/10.1016/j.commatsci.2018.03.069 https://www.sciencedirect.com/science/article/pii/S0927025618302283.
[19] H. Song, M. Wang, Q. Deng, Y. Li, Deformation mode transitions in cu50zr50 amorphous/cu crystalline nanomultilayer: a molecular dynamics study, J. Non-Cryst. Solids 490 (2018) 13–21 https://doi.org/10.1016/j.jnoncrysol.2018.03.036 http://www.sciencedirect.com/science/article/pii/S0022309318301558.
[20] S. Pauly, G. Liu, G. Wang, U. Khn, N. Mattern, J. Eckert, Microstructural heterogeneities governing the deformation of cu47.5zr47.5al5 bulk metallic glass composites, Acta Mater. 57 (18) (2009) 5445–5453 https://doi.org/10.1016/j.actamat.2009.07.042 http://www.sciencedirect.com/science/article/pii/S1359645409004765.
[21] H.C. Sun, Z.L. Ning, G. Wang, W.Z. Liang, S. Pauly, Y.J. Huang, S. Guo, X. Xue, J.F. Sun, In–situ tensile testing of zrcu-based metallic glass composites, Sci. Rep. 8 (2018) 4651, https://doi.org/10.1038/s41598-018-22925-2 https://www.nature.com/articles/s41598-018-22925-2.
[22] D. Şopu, M. Stoica, J. Eckert, Deformation behavior of metallic glass composites reinforced with shape memory nanowires studied via molecular dynamics simulations, Appl. Phys. Lett. 106 (21). doi:https://doi.org/10.1063/1.4921857. URL http://scitation.aip.org/content/aip/journal/apl/106/21/10.1063/1.4921857.
[23] Y.W. Luan, C.H. Li, X.J. Han, J.G. Li, Plastic deformation behaviours of cuzr amorphous/crystalline nanolaminate: a molecular dynamics study, arXiv:https://doi.org/10.1080/08927022.2017.1328554, Mol. Simulat. 43 (13–16) (2017) 1116–1124, https://doi.org/10.1080/08927022.2017.1328554 https://doi.org/10.1080/08927022.2017.1328554.
[24] T. Brink, M. Peterlechner, H. Rösner, K. Albe, G. Wilde, Influence of crystalline nanoprecipitates on shear-band propagation in cu-zr-based metallic glasses, Phys. Rev. Appl. 5 (2016) 054005https://doi.org/10.1103/PhysRevApplied.5.054005 https://link.aps.org/doi/10.1103/PhysRevApplied.5.054005.
[25] C. Kalcher, T. Brink, J. Rohrer, A. Stukowski, K. Albe, Interface-controlled creep in metallic glass composites, Acta Mater. 141 (2017) 251–260 https://doi.org/10.1016/j.actamat.2017.08.058 http://www.sciencedirect.com/science/article/pii/S135964541730722X.
[26] M. Sepulveda-Macias, N. Amigo, G. Gutierrez, Tensile behavior of cu50zr50 metallic glass nanowire with a b2 crystalline precipitate, Phys. B Condens. Matter 531 (2018) 64–69 https://doi.org/10.1016/j.physb.2017.12.005 http://www.sciencedirect.com/science/article/pii/S0921452617309900.
[27] Y.Q. Cheng, E. Ma, H.W. Sheng, Atomic level structure in multicomponent bulk metallic glass, Phys. Rev. Lett. 102 (2009) 245501, https://doi.org/10.1103/PhysRevLett.102.245501 https://link.aps.org/doi/10.1103/PhysRevLett.102.245501.
[28] M.S. Daw, M.I. Baskes, Semiempirical, quantum mechanical calculation of hydrogen embrittlement in metals, Phys. Rev. Lett. 50 (1983) 1285–1288, https://doi.org/10.1103/PhysRevLett.50.1285 https://link.aps.org/doi/10.1103/PhysRevLett.50.1285.
[29] J. Ding, Y. Cheng, E. Ma, Full icosahedra dominate local order in cu64zr34 metallic

glass and supercooled liquid, Acta Mater. 69 (2014) 343–354 https://doi.org/10.1016/j.actamat.2014.02.005 http://www.sciencedirect.com/science/article/pii/S1359645414000858.
[30] Y.C. Hu, F.X. Li, M.Z. Li, H.Y. Bai, W.H. Wang, Five-fold symmetry as indicator of dynamic arrest in metallic glass-forming liquids, Nat. Commun. 6 (2015) 8310 EP–, article https://doi.org/10.1038/ncomms9310.
[31] J. Ding, Y.Q. Cheng, H. Sheng, M. Asta, R.O. Ritchie, E. Ma, Universal structural parameter to quantitatively predict metallic glass properties, Nat. Commun. 7 (2016) 13733 EP –, article https://doi.org/10.1038/ncomms13733.
[32] S. Plimpton, Fast parallel algorithms for short-range molecular dynamics, J. Comput. Phys. 117 (1) (1995) 1–19 https://doi.org/10.1006/jcph.1995.1039 http://www.sciencedirect.com/science/article/pii/S002199918571039X.
[33] M. Sepulveda-Macias, N. Amigo, G. Gutierrez, Onset of plasticity and its relation to atomic structure in cuzr metallic glass nanowire: a molecular dynamics study, J. Alloy. Comp. 655 (2016) 357–363 https://doi.org/10.1016/j.jallcom.2015.09.149 http://www.sciencedirect.com/science/article/pii/S0925838815311257.
[34] N. Amigo, M. Sepulveda-Macias, G. Gutierrez, Martensitic transformation to monoclinic phase in bulk b2cuzr, Intermetallics 91 (2017) 16–21 https://doi.org/10.1016/j.intermet.2017.08.003 http://www.sciencedirect.com/science/article/pii/S0966979517305964.
[35] M. Sepulveda-Macias, G. Gutierrez, F. Lund, Strain rate and temperature effect on zr 50 cu 50 metallic glass under pure shear, J. Phys. Conf. 1043 (1) (2018) 012040http://stacks.iop.org/1742-6596/1043/i=1/a=012040.
[36] F. Shimizu, S. Ogata, J. Li, Theory of shear banding in metallic glasses and molecular dynamics calculations, Mater. Trans. 48 (11) (2007) 2923–2927.
[37] Y.Q. Cheng, A.J. Cao, E. Ma, Correlation between the elastic modulus and the intrinsic plastic behavior of metallic glasses: the roles of atomic configuration and alloy composition, Acta Mater. 57 (11) (2009) 3253–3267 https://doi.org/10.1016/j.actamat.2009.03.027 http://www.sciencedirect.com/science/article/pii/S1359645409001906.
[38] C.L. Kelchner, S.J. Plimpton, J.C. Hamilton, Dislocation nucleation and defect structure during surface indentation, Phys. Rev. B 58 (1998) 11085–11088, https://doi.org/10.1103/PhysRevB.58.11085 https://link.aps.org/doi/10.1103/PhysRevB.58.11085.
[39] A. Stukowski, Visualization and analysis of atomistic simulation data with ovitothe open visualization tool, Model. Simulat. Mater. Sci. Eng. 18 (1) (2010) 015012http://stacks.iop.org/0965-0393/18/i=1/a=015012.
[40] Y. Wu, D. Ma, Q. Li, A. Stoica, W. Song, H. Wang, X. Liu, G. Stoica, G. Wang, K. An, X. Wang, M. Li, Z. Lu, Transformation-induced plasticity in bulk metallic glass composites evidenced by in-situ neutron diffraction, Acta Mater. 124 (2017) 478–488 https://doi.org/10.1016/j.actamat.2016.11.029 http://www.sciencedirect.com/science/article/pii/S1359645416308965.